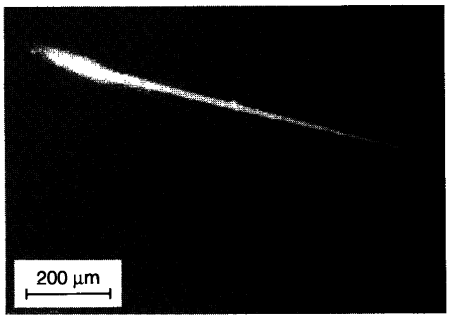

Fig. 5. An optical micrograph of the realization of two waveguides scratched according to Fig. 4. A laser beam is coupled into the upper one, leading to a bright streak of collimated light as a result of the waveguiding properties. The waveguides are 6 μm wide and 5 mm long.

What happens to the refractive index as one moves perpendicularly in z direction, away from the scratched surface? In region 2, the refractive index in the y direction decreases with increasing z because of the TN alignment of the LC molecules. Light cannot escape in the z direction because it is bent back, analogous to a graded-index waveguide.

We fabricated such structures (Fig. 4) with the home-built instrument by scratching a suitable pattern 6 μm wide and 5 mm long. To prevent the formation of reverse twist domains, we selected θ slightly smaller than 90°. The light-guiding property of this structure was deduced from the observation of a streak of light when a laser beam was suitably coupled into it (Fig. 5). The fabrication of this waveguide demonstrates that we can design bulk refractive index patterns by well-defined scratching patterns made with the SFM. Preliminary results on the possibility of fabricating coupling gratings, beam splitters, and other optical structures indicate that the smallest dimension of index patterns feasible is determined by elastic properties of the LC molecules as well as inhomogeneities of the polymer substrate but not by the size of the scratched areas.

We expect that this technique of writing an orientation pattern with a tip of an SFM will trigger the development of new devices because it offers a flexibility in shaping refractive index profiles that is unmatched by other techniques, such as photolithography-based pattern generation. The possibility provided by the SFM patterning technique to form arbitrarily complex two- or even three-dimensional refractive index patterns will certainly find further applications.

REFERENCES AND NOTES

1. K. Schmitt *et al.*, *Liq. Cryst.* **14**, 1735 (1993); K. Schmitt *et al.*, *J. Phys. III* **4**, 387 (1994).
2. For a review, see D. Rugar and P. Hansma, *Phys. Today* **43**, 23 (October 1990).
3. D. W. Berreman, *Phys. Rev. Lett.* **28**, 1683 (1972); J. M. Geary *et al.*, *J. Appl. Phys.* **62**, 4100 (1987); J. A. Castellano, *Mol. Cryst. Liq. Cryst.* **94**, 33 (1983); E. S. Lee, Y. Saito, T. Uchida, *Jpn. J. Appl. Phys.* **32**, L1822 (1993).
4. Th. Jung *et al.*, *Ultramicroscopy* **42**, 1446 (1992); E. Hamada and R. Kaneko, *ibid.*, p. 184; R. Kaneko and E. Hamada, *Wear* **162**, 370 (1993); X. Jin and W. N. Unertl, *Appl. Phys. Lett.* **61**, 657 (1992); O. M. Leung and M. C. Goh, *Science* **255**, 64 (1992).
5. H. Kado, K. Yokoyama, T. Tohda, *Rev. Sci. Instrum.* **63**, 3330 (1992).
6. Nanoscope III from Digital Instruments, Santa Barbara, CA.
7. The authors thank R. Lüthi, H. Haefke, L. Howald, and E. Meyer for helpful discussions. P.G. thanks the Treubel Fonds, Basel, for generous financial support. This research is supported by the Swiss National Science Foundation and the Kommission zur Förderung der wissenschaftlichen Forschung.

14 March 1994; accepted 31 May 1994

Measurement of Laser-Plasma Electron Density with a Soft X-ray Laser Deflectometer

D. Ress,* L. B. DaSilva, R. A. London, J. E. Trebes, S. Mrowka, R. J. Procassini, T. W. Barbee Jr., D. E. Lehr

A soft x-ray laser (wavelength λ = 15.5 nanometers) was used to create a moiré deflectogram of a high-density, laser-produced plasma. The use of deflectometry at this short wavelength permits measurement of the density spatial profile in a long-scalelength (3 millimeters), high-density plasma. A peak density of 3.2×10^{21} per cubic centimeter was recorded.

A detailed knowledge of the electron density spatial distribution in a laser-produced plasma is required in a wide range of scientific endeavors such as inertial confinement fusion (*1*), laser-plasma interaction physics (*2*), and high-temperature and high-density laboratory astrophysics (*3*). Density information is currently obtained with such diverse techniques as x-ray spectroscopy (*4*), absorption and scattering of incident laser light (*5*), and ultraviolet interferometry (*6*). All of these techniques are useful over only a limited range of densities and scale sizes, and they have additional limitations. Measurements based on x-ray spectroscopic techniques suffer from uncertainties in opacity and usually require sophisticated modeling of the atomic processes occurring in the plasma to infer a density. Measurements based on laser-light scattering require an understanding of one or more parametric instabilities produced by the laser creating the plasma under study. Ultraviolet interferometry is restricted to density length products less than 2×10^{19} cm^{-2}, forcing high-density measurements to be made on plasmas with sizes that are often too small to be of interest.

To overcome some of these limitations, we have developed a technique based on moiré deflectometry (*7*) with a soft x-ray laser beam. We used this method to measure the electron density profile in a 3-mm-diameter laser-produced plasma. The maximum density length product measured was 9.6×10^{20} cm^{-2}, about 50 times higher than could be measured with conventional ultraviolet interferometry. The line-averaged peak density of 3.2×10^{21} cm^{-3} was limited by diffraction effects associated with the steepness of the density profile. Higher densities can be accessed by modifying the experimental arrangement.

When a high-intensity ($I > 10^{13}$ W/cm^2) laser irradiates a solid target, a plasma is created. The transverse extent of these plasmas is determined by the laser spot size and typically varies from hundreds to thousands of micrometers in diameter. The index of refraction for light propagating through this plasma is given by

$$N = \sqrt{1 - n_e/n_c} \qquad (1)$$

where n_e is the electron density, $n_c = 1.1 \times 10^{27}/\lambda^2$ is the critical electron density per cubic centimeter, and λ is the wavelength of the light in nanometers. Because the laser beam can only propagate in the plasma where $n_e < n_c$, we can readily distinguish two regions in the direction normal to the material surface. The overdense region is where $n_e > n_c$, and the corona is where $n_e < n_c$. In our experiments, we used a green (λ = 527 nm) laser drive beam with $n_c = 4 \times 10^{21}$ cm^{-3}. In the corona, at densities close to but less than critical, the spatial profile maintains a constant shape (steady-state profile) that slowly moves outward from the disk surface at a speed on the order of 10^6 cm/s (*8*). At lower densities, the spatial profile changes with time in a self-similar fashion. The profile here is a decaying exponential with a scalelength that

D. Ress, L. B. DaSilva, R. A. London, J. E. Trebes, S. Mrowka, R. J. Procassini, T. W. Barbee Jr., Lawrence Livermore National Laboratory, Livermore, CA 94551–5508, USA.
D. E. Lehr, Physics Department, Stanford University, Stanford, CA 94305, USA.

*To whom correspondence should be addressed.

increases linearly with time. The boundary between steady-state and self-similar behavior moves outward to lower densities as time advances (9). We confined our measurements to this steady-state portion of the coronal density profile to avoid temporal blurring.

Moiré deflectometry has been used extensively to measure a variety of physical phenomena. It is a relatively recent technique that yields optical phase information similar to that obtained in interferometry. Deflectometry has been used to do routine characterization of optical components and dynamical studies of fluid flow (7). It has also been used to measure plasma density variations (10). We formed a deflectogram with short wavelength radiation ($\lambda = 15.5$ nm) produced by a yttrium soft x-ray laser. The short wavelength allows density measurements in millimeter-scale laser-produced plasmas at densities exceeding 10^{21} cm^{-3}.

Deflectometry measures the refraction of a collimated beam of light through a subject. There are a variety of methods available to measure refraction, such as Schlieren imaging (11) and grid-image refractometry (12). Schlieren techniques provide information about the positions of highly refractive density interfaces but, unlike deflectometry, not about the magnitudes of the density changes across the interfaces. Grid-image refractometry provides a measurement very similar to deflectometry. Used with a soft x-ray light source, grid-image refractometry could also allow characterization of long-scalelength, laser-produced plasma.

Let us describe the collimated beam of radiation (probe beam) as a set of rays. The index-of-refraction gradient in the plasma bends the rays through an angle

$$\phi = \int_{-\infty}^{s_0} ds \frac{dN}{dx} \qquad (2)$$

where the integration is carried out along the path of the ray s and we assume that the plasma varies only in the x direction (normal to the target surface).

A soft x-ray beam is necessary to probe millimeter-scale laser-produced plasmas. Previous deflectometry and interferometry efforts that used visible and ultraviolet wavelength probe beams were limited by excessive refraction. For a uniform-slab plasma of length L, we can approximate for $n_e/n_{cp} \ll 1$

$$\phi \approx -\frac{1}{2}\frac{n_e}{n_{cp}}\frac{L}{L_t} \qquad (3)$$

where the transverse (to the probe beam) density gradient scalelength is

$$L_t = \left[\frac{1}{n_e}\frac{\partial n_e}{\partial x}\right]^{-1} \qquad (4)$$

and the critical density for the probe radiation is n_{cp}. From hydrodynamical modeling, we expect that L_t is as small as 20 μm in the corona; we assume that $L = 1$ mm. For $\lambda = 260$ nm, we can get $\phi \gg 1$, and the probe beam will be too severely refracted to allow a sensible measurement. In contrast, for $\lambda = 15.5$ nm, we get $\phi \approx 0.1$, an acceptable amount of refraction. A soft x-ray laser (13) provides the desired short wavelength probe beam.

A moiré pattern is created when a probe beam is passed through a pair of rotationally offset (angle θ) one-dimensional rulings consisting of evenly spaced (spacing p) opaque and transmissive stripes. The moiré pattern (Fig. 1) is a set of dark regions that correspond to the intersections of the stripes and lighter regions that are the rhomboid-shaped open areas in between. In normal operation the high spatial frequency variations are not resolved, and we observe a smooth set of moiré fringes. The spacing of the fringes is given by the ratio p/θ.

When a refracted probe beam passes through the rulings, the moiré fringes are shifted by a distance $\Delta s = d\phi/\theta$, where d is the separation between the two rulings. At large x, $N = 1$ and $\partial N/\partial x = 0$ because n_e is negligible. Thus, a straight line can be fit to the fringe paths at large x, and the deviation from this line gives the angular deflection as a function of position as we move toward the target surface. If we assume the plasma to be one dimensional and integrate from unity at large x, we can determine the index-of-refraction profile. In our experiment, the spot size is so large ($L \gg L_t$) that the plasma density variation is nearly one dimensional.

We controlled the sensitivity of the deflectometer by varying the distance separating the rulings. In practice, diffraction limits the allowable values for d. At multiples of a particular distance, $d_t = p^2/\lambda$, where λ is the probe beam wavelength, the first ruling is self-imaged onto the second ruling. For spacings midway between multiples of d_t, the contrast between the moiré fringes decreases to zero (14).

We produced an x-ray laser probe beam by irradiating an yttrium foil with 531-nm light from one of the Nova beams (Fig. 2). The x-ray laser typically delivered about 7 mJ of energy at 15.5 nm in a beam that diverged at a 5-mrad half angle (15). The pulse duration was 150 to 200 ps, which was short enough to avoid temporal blurring.

We created the target plasma with a second Nova laser beam, which irradiated the planar target, a 5-mm-square, 50-μm-thick polyethylene (CH) disk. To create a relatively gentle electron density profile and minimize x-ray self-emission, we irradiated the target at a low intensity, $I \approx 2.5 \times 10^{13}$ W/cm^2. The laser pulse was a 1-ns-long, temporally square pulse, delivering a total energy of 1.8 kJ. The x-ray probe beam passed through the target plasma 0.9 ns after the start of the irradiation. To maximize the observed fringe deflections and demonstrate the capability to probe relatively long plasmas, we used a large, 3-mm-diameter laser spot.

To transport the x-ray laser to the target plasma and image the illuminated target plane, we used a sequence of multilayer

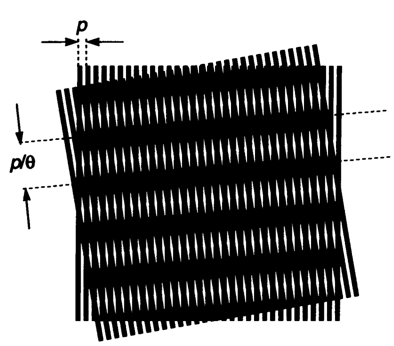

Fig. 1. A moiré pattern is produced by overlaying two rotationally offset one-dimensional rulings.

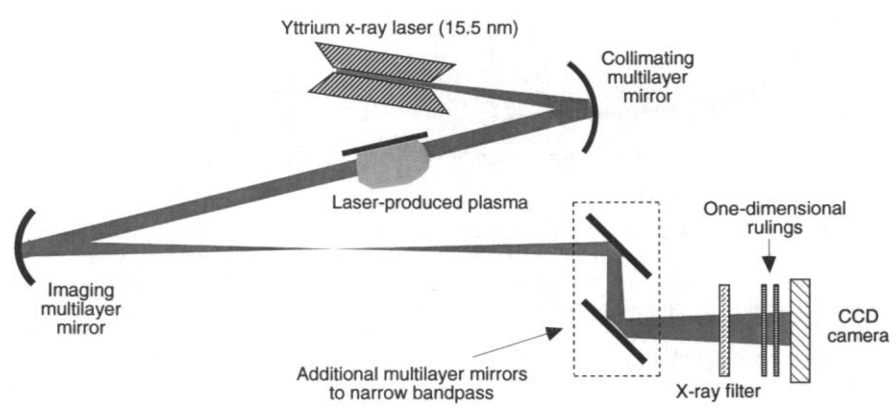

Fig. 2. Experimental arrangement for the plasma density measurements.

mirrors (Fig. 2) with reflectivity ≥50%. The x-ray laser beam first traveled 50 cm to a 2.5-cm-diameter spherical mirror, which produced a collimated probe beam 5 mm in diameter. After propagating another 50 cm, the probe illuminated the laser-plasma target. The target plasma was imaged by a spherical mirror focused at the center of the plasma. The image formed by this mirror was relayed by two 45° flat mirrors to a detector plane at a magnification of 10. The image also passed through a filter consisting of 100-nm-thick Al and 100-nm-thick Ti on a 200-nm-thick plastic substrate. The combination of mirrors and a filter produced a narrow photon passband (0.5-nm bandwidth) centered at 15.5 nm.

The moiré pattern was formed by passing the image through a pair of 200-nm-thick gold bar rulings with spacing $p = 10$ μm and rotational offset $\theta = 4°$ to give a fringe spacing of 142 μm in the image plane (14.2 μm at the object plane). The bars were oriented parallel to the disk target surface so that the deflectogram would reveal density variations normal to the disk surface. The rulings were separated by a distance $3d_t$ = 19.35 mm to give a sensitivity of 5.2 mrad per fringe shift at the object plane.

We recorded the resulting moiré deflectogram with an x-ray–sensitive charge-coupled device (CCD) camera. The CCD camera used a 1024 × 1024 chip illuminated through its thinned backside and had an efficiency of 3.4 electrons per photon at λ = 15.5 nm.

As a control experiment, we created a deflectogram using the x-ray laser probe beam without the laser-produced plasma. The image (Fig. 3A) shows a uniform and unperturbed moiré pattern throughout, except where the beam was blocked by the CH target. The fringe contrast $(I_{max} - I_{min})/(I_{max} + I_{min})$ is 0.43, as compared to the theoretical maximum of 0.67. The contrast was probably reduced by ruling imperfections.

In our second experiment, we created a deflectogram of a CH plasma. The image (Fig. 3B) shows the expected unperturbed moiré pattern in areas that are far from the laser-illuminated surface. Closer to the surface there are distinct deflections as large as 3.9 fringe spacings, corresponding to a refracted angle of about 20 mrad.

Immediately adjacent to the disk surface, the fringes disappear and the image intensity is fairly uniform. We expect a loss of fringe contrast here because of the strong density gradients near the critical surface of the plasma. The density gradient limitations can be reduced by increasing the system magnification and reducing the ruling separation.

Soft x-ray deflectometry can be carried out with much weaker sources than our yttrium soft x-ray laser. The deflectogram obtained in our experiment had a very high peak signal level, about 10^4 electrons per pixel, as compared with the noise level of about 20 electrons per pixel. For acceptable image quality, the signal-to-noise ratio should be at least 20, so our incident x-ray laser intensity could have been reduced by a factor of 25. System throughput could also be improved by about a factor of 10 by reducing the thickness of the filters and replacing the pair of 45° incidence mirrors with a single normal incidence mirror. It should therefore be possible to produce a deflectogram with any source of collimated x-rays with an energy greater than 30 μJ. Such fluences should be available from lower energy x-ray laser systems such as selenium or germanium. This method is not confined to x-ray laser illumination sources but can be used with synchrotron x-ray sources as well.

For analysis of the deflectogram, a computer program was written to track the fringe positions. A set of straight lines is fit to the fringe trajectories in an unperturbed portion of the image. The same fringes are tracked into the perturbed portion of the image, and deviations from the straight lines are calculated and converted to angular deflection. There is little variation in the deflection profiles of 11 adjacent fringes (Fig. 4A), verifying the one-dimensional nature of the density profile.

Figure 4B shows the density profile obtained by this method. Because the fringe deflections in Fig. 4A are so repeatable, we used the average deflection to further reduce noise. There is a ±20-μm uncertainty in the absolute position of the profile because no spatial fiducial point is presently available to accurately identify the original position of the disk surface. The relative error in density decreases as the density increases because of the averaging associated with the numerical integration.

To design the initial target plasma and to compare with measured density profiles, we have done numerical hydrodynamics simulations with the LASNEX computer code (*16*). We used a one-dimensional "spherical cap" geometry to simulate the divergence of the plasma as it expands. The model was similar to the one used in much previous work (*2*, *8*). The electron density profiles produced by the LASNEX model were then used as input to a three-dimensional ray-tracing code (*17*) that calculated the refraction of a soft x-ray probe beam through the plasma.

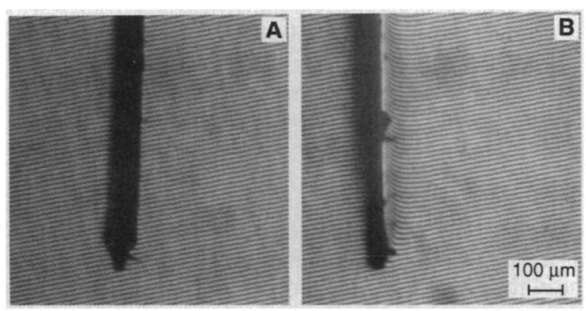

Fig. 3. Two deflectograms were produced by the experiments. (**A**) Control image showing unperturbed moiré pattern; (**B**) plasma deflectogram showing deflections of >3.5 fringe spacings. The features in the image close to the target surface are probably caused by ripples in the CH material.

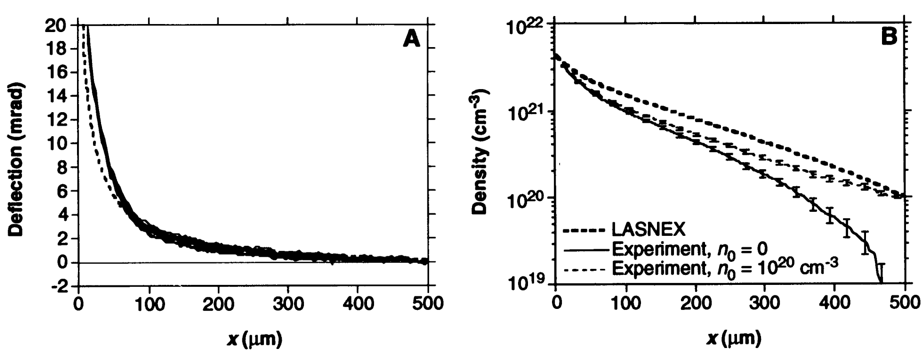

Fig. 4. Analysis of the plasma deflectogram. (**A**) Deflection profile. We chose a region near the center of the image where the target surface was relatively flat. Deflections obtained from 11 adjacent fringes in this region are overlaid in the figure. The curves are extremely similar, indicating a one-dimensional plasma density profile. (**B**) Density profile. We obtained the density from the average of the fringe deflections in (A). The fundamental error in the measurement corresponds to $1/2\pi$ of a fringe spacing, reduced by a factor of $\sqrt{11}$ by the averaging of 11 fringe profiles. The error decreases as the density increases because the numerical integration corresponds to the averaging of multiple independent measurements. The two experimental curves that are plotted correspond to assumed initial densities of 0 and 10^{20} cm^{-3}.

A set of 201 rays were launched parallel to the initial target surface; they then traversed the simulated plasma represented by the LASNEX output. The ray deflections were calculated from the LASNEX density profile with Eqs. 1 and 2. Only gradients perpendicular to the target surface were considered; the plasma was assumed to be azimuthally uniform with an initial diameter of 3 mm.

The code results for deflection are compared with the measurements in Fig. 4A. The ray-tracing calculation was carried out with use of the simulated density profile obtained 0.9 ns after the start of the laser pulse that created the target plasma; this corresponds to the peak of the x-ray laser probe beam. The measured deflections show good agreement with theory. The simulation results do predict a very slightly larger deflection at large distances from the target surface.

To compare the LASNEX prediction of the density profile to the experiment, we integrated the index-of-refraction gradient profile. The slope normalization in the deflectogram was carried out at as far from the target surface as possible, but at about $x = 500\ \mu m$, we needed to make some assumption about the boundary density n_0. We could have assumed the density here to be zero, but LASNEX modeling indicated that the density at $x = 500\ \mu m$ is $\sim 10^{20}\ cm^{-3}$. Therefore, we plotted two curves, one corresponding to $n_0 = 0$ and another for $n_0 = 10^{20}\ cm^{-3}$ (Fig. 4B). There is substantial disagreement between the code prediction and the $n_0 = 0$ curve, but the $n_0 = 10^{20}$ curve agrees with the simulation to within about 40% throughout the corona. At low densities ($n_e < 10^4\ cm^{-3}$) the uncertainty regarding the initial density at the edge of the deflectogram does not presently allow a final comparison with the code predictions; later experiments with increased field-of-view and sensitivity will be required to resolve this issue. At higher densities, the 40% disagreement exceeds the measurement uncertainties. The LASNEX calculations appear to overestimate the electron density in the steady-state part of the corona, confirming comparisons with earlier experiments (8).

REFERENCES AND NOTES

1. J. D. Lindl *et al.*, *Phys. Today* **45**, 32 (September 1992); J. H. Nuckolls *et al.*, *Nature* **239**, 139 (1972).
2. R. P. Drake *et al.*, *Phys. Fluids* **31**, 3130 (1988); C. L. Shepard *et al.*, *ibid.* **29**, 584 (1986); W. C. Mead *et al.*, *ibid.* **26**, 2316 (1983).
3. L. B. Da Silva *et al.*, *Phys. Rev. Lett.* **69**, 438 (1992).
4. J. F. Seely *et al.*, *J. Quant. Spectrosc. Radiat. Transfer* **27**, 297 (1982); C. De Michelis and M. Mattioli, *Nucl. Fusion* **21**, 677 (1981).
5. R. P. Drake *et al.*, *Phys. Fluids B* **1**, 1089 (1989); H. Figuroa, C. Joshi, H. Azechi, N. A. Ebrahim, K. G. Estabrook, *Phys. Fluids* **27**, 1887 (1984).
6. G. E. Busch, C. L. Shepard, L. D. Siebert, J. A. Tarvin, *Rev. Sci. Instrum.* **56**, 879 (1985).
7. O. Kafri and I. Glatt, *The Physics of Moiré Metrology* (Wiley, New York, 1990).
8. E. F. Gabl *et al.*, *Phys. Fluids B* **2**, 2437 (1990); D. Ress, L. J. Suter, E. F. Gabl, B. H. Failor, *ibid.*, p. 2448.
9. R. F. Schmalz and K. Eidmann, *Phys. Fluids* **29**, 3483 (1986); R. F. Schmalz, *ibid.* **28**, 2923 (1985).
10. T. Afshar-Rad *et al.*, *Phys. Rev. Lett.* **68**, 942 (1992); J. S. Schlacter, *Tech. Rep. LA-9333-T* (Los Alamos National Laboratory, Los Alamos, NM, 1982).
11. L. A. Vasil'ev, *Schlieren Methods* (Israel Program for Scientific Translations, New York, 1971).
12. R. S. Craxton *et al.*, *Phys. Fluids B* **5**, 4419 (1993); C. Darrow *et al.*, *J. Appl. Phys.* **67**, 3630 (1990).
13. R. C. Elton, *X-Ray Lasers* (Academic Press, Boston, MA, 1990).
14. E. Keren and O. Kafri, *J. Opt. Soc. Am. A* **2**, 111 (1985).
15. L. B. DaSilva *et al.*, *Opt. Lett.* **18**, 1174 (1993).
16. G. B. Zimmerman and W. L. Kruer, *Comments Plasma Phys. Controlled Fusion* **2**, 85 (1975). LASNEX is primarily a hydrodynamic simulation code. The dynamics of a hot fluid are modeled by a finite-difference solution of Euler's equations. The code also models the deposition of laser energy in the plasma by inverse bremsstrahlung, the transport of x-rays through the material by diffusion, and electron thermal conduction by diffusion.
17. M. K. Prasad *et al.*, *Phys. Fluids B* **4**, 1569 (1992).

18. We gratefully acknowledge the assistance of D. Ciarlo in fabricating the one-dimensional rulings and the Nova two-beam laser-facility crew for performing these experiments. This work was performed under the auspices of the U.S. Department of Energy by Lawrence Livermore National Laboratory under contract W-7405-ENG-48.

23 February 1994; accepted 24 May 1994

Contribution of Early Cells to the Fate Map of the Zebrafish Gastrula

Kathryn Ann Helde,* Ellen T. Wilson,* Chris J. Cretekos, David Jonah Grunwald†

Previously, a tissue-specific fate map was compiled for the gastrula stage of the zebrafish embryo, indicating that development subsequent to this stage follows a reproducible pattern. Here it is shown that each early zebrafish blastomere normally contributes to a subset of the gastrula and thus gives rise to a limited array of tissues. However, the final contribution that any early blastomere makes to the fate map in the gastrula cannot be predicted because of variability in both the position of the future dorsoventral axis with respect to the early cleavage blastomeres and the scattering of daughter cells as the gastrula is formed. Therefore, early cell divisions of the zebrafish embryo cannot reproducibly segregate determinants of tissue fates.

Defining how and when cell fate is determined is essential to understanding the mechanisms underlying development. In the zebrafish embryo, cell lineage analysis has shown that it is not until the early gastrula stage that cellular fate appears restricted, in that individual cells give rise to only single tissue types (*1*). The type of tissue formed by the descendants of an early gastrula cell can be generally predicted by the position of the cell within the early gastrula embryo, yielding a fate map for the zebrafish (*2*) (Fig. 1A). Because a tissue-specific fate map cannot be derived before this stage and there is little cell movement during the cleavage period, it has been proposed that extensive cell mixing occurs during the transition from blastula to gastrula (*3, 4*), such that a cell's position in the blastula is unrelated to the position of its descendants in the gastrula. In this model, the early blastomeres of the zebrafish are deemed to be pluripotent. Recent cell lineage results have challenged the idea that extensive mixing occurs, suggesting that the position of an early blastomere is a reliable predictor of some aspects of later cell fate (*5*). A further conclusion from the latter work was that the body axes of the embryo can be predicted as early as the eight-cell stage. Here we resolve the issue of how the position of a cleavage blastomere relates to the distribution of its clonal descendants in the gastrula. We demonstrate that descendants of early blastomeres do not have predictable positions relative to the dorsoventral axis of the embryo. Thus, their prospective fates are not identifiable. In addition, we demonstrate that portions of the embryo retain their relative positions from blastula to gastrula, allowing some aspects of the zebrafish fate map to be observable at times earlier than the gastrula stage.

In the gastrula, a cell's position relative to the dorsal midline and along the animal-vegetal axis allows the fate of that cell to be predicted (Fig. 1A). For example, cells at the dorsal margin of the early gastrula have a specialized role in organizing the primary axis of the embryo (*6*). We have directly tested whether the position of early blastomeres correlates with the dorsoventral

Department of Human Genetics, Eccles Institute of Human Genetics, University of Utah, Salt Lake City, UT 84112, USA.

*These colleagues contributed equally to this work.
†To whom correspondence should be addressed.